Application of Parametric Airfoil Design for Rotor Performance Improvement

Joon W. Lim
US Army Aviation Development Directorate
Aviation & Missile Research, Development & Engineering Center
Ames Research Center, Moffett Field, CA

ABSTRACT

A parametric airfoil design tool, PARFOIL, has been developed in a framework of rotor optimization. The design parameters in PARFOIL include camber and its crest position, thickness and its crest position, leading edge radius, trailing edge camber and its crest position, and boat-tail angle. Upon replacing the standard SC airfoils (SC1095 and SC1094R8) with the advanced RC airfoils (RC(3)-08 and RC(4)-10NL), a sensitivity study with design parameters is performed for UH-60A rotor performance. Camber crest position is found the most influential design parameter. Based on the outcomes in the sensitivity study, new rotor blade configurations are designed and examined for performance improvement. In comparison with the UH-60A standard rotor configuration, it is found that the performance-based best rotor reduces power required by 3.2% in hover, 11.3% at μ=0.3, and 13.6% at μ=0.4. This demonstrates the ability of PARFOIL to produce better airfoils in the design space. In spite of the performance improvements, the pitch link load of the performance-based best rotor shows an increase of about 8.5% from the UH-60A standard rotor configuration for the UTTAS high-g pull-up condition, which indicates the need to consider pitch link load under high thrust condition as a constraint in the blade design process.

NOTATION

b	Boat tail angle, deg
BL	UH-60A rotor having advanced RC airfoils as a baseline
c_d	Drag coefficient
c_m	Moment coefficient
c_p	Power coefficient
c	Airfoil chord
f_k	Scaling factor for leading edge radius
f_m	Scaling factor for camber
k	Leading edge radius in chords
m	Camber in chords
M_{dd}	Drag divergence Mach number
n	Trailing edge camber in chords
p	Camber crest position in chords
q	Trailing edge camber crest position in chord
STD	UH-60A standard rotor
t	Airfoil thickness in chords
X	Propulsive force, lbs
x	Airfoil thickness crest position in chords
y_b	Horizontal position of boat-tail angle in chords
y	Airfoil horizontal coordinate in chords

INTRODUCTION

There have been numerous activities of developing advanced rotorcraft around the world. The designs range from small-scale drones and Unmanned Aerial Vehicles (UAV) to large-scale Joint Multi-Role (JMR)/Future Vertical Lift (FVL) aircraft [1-4]. As demands for advanced rotorcraft grow, the need for advanced airfoil design increases. But, the airfoil design process of rotorcraft manufacturers has not been usually disclosed and in the rotorcraft research community an ad hoc approach has often been part of the airfoil design process.

Airfoil parameterization methods have been widely used in the fixed wing industry. PARSEC (**Par**ameterized **Sec**tion) is a well-accepted parametric airfoil design tool introduced by Sobieczky [5]. This tool constructs airfoil ordinates by blending eleven design parameters using polynomial fitting (up to sixth order) and spline interpolation. A majority of the design methods are based on design parameters that are intuitive and physical.

Another common parameterization method is the CST (**C**lass function/**S**hape function **T**ransformation) method introduced by Kulfan [6]. This method is based heavily on mathematical interpolation polynomials. The class function defines fundamental classes of airfoils, axisymmetric bodies, and axisymmetric nacelle geometries, and the shape function defines unique geometric shapes within each fundamental class. This method decomposes airfoil shape function into component airfoils that are represented by Bernstein polynomials. Both the PARSEC and the CST methods are frequently seen within the framework of wing aerodynamic optimization. There are available numerous other airfoil parameterization methods [7-8] in addition to these two methods.

MASSOUD [9] is a **M**ultidisciplinary **A**erodynamic-**S**tructural **S**hape **O**ptimization tool **U**sing **D**eformation and performs parameterizations

Presented in the 44th European Rotorcraft Forum, September 18-21, 2018, Delft, Netherlands.

not only for blade airfoils but also for rotor blade planform by means of shape perturbations and a soft object animation algorithm. Design parameters include airfoil thickness and camber, blade twist, dihedral, and other blade planform parameters. Wang [10] *et al.* successfully demonstrated a 3.2% torque reduction for the HART II rotor in descent flight using MASSOUD.

The use of advanced airfoils is essential for optimal rotor performance. Advanced airfoils designed for rotor performance would perform well for compressibility on the advancing side and for stall on the retreating side. By replacing the airfoils on the UH-60A rotor blade to an ad-hoc choice of advanced airfoils, Lim [11] showed that rotor power reduced 7.3% at μ=0.3 and 12.1% at μ=0.4 (see Fig. 1). This sizable improvement does not imply that the blade is optimized for rotor performance with respect to airfoil selection. To achieve an optimal blade design while satisfying design constraints, a parametric airfoil design tool that provides a series of morphed airfoil geometries needs to be used in conjunction with a numerical optimizer.

The objectives of this paper are: 1) to develop a methodology of parametric airfoil design in a framework of rotor optimization, and 2) to acquire an understanding of the sensitivity of airfoil design parameters for performance improvement of the UH-60A rotor. The parametric sensitivity analysis used in this paper does not employee a formal optimization technique but helps select the desired airfoil geometries that improve rotor performance in the design space of interest.

PARAMETRIC AIRFOIL DESIGN

A parameterization method for an airfoil geometry affects numerical efficiency in the optimization process. Typically, an airfoil geometry is parameterized using a number of design parameters in order to control or morph airfoil coordinates. An efficient parametric model can be expressed with a small number of design parameters in a large design space of interest and a good choice of design parameters allows easy and intuitive modification of airfoil coordinates.

A **par**ametric air**foil** method (PARFOIL) has been developed based on typical airfoil design parameters such as camber, thickness, or leading edge radius. Unlike other methods, PARFOIL performs a parameterization starting from a baseline airfoil geometry and then morphing it to a desired airfoil geometry by means of augmenting the design parameters. The baseline airfoil is chosen typically as the airfoil that one would like to improve. Although the outcomes of parametric airfoil design tools would be similar, PARFOIL could generate desired airfoil geometries more effectively by taking advantage of the shape of the selected airfoil geometry.

Prior to parameterization, redistribution of grid points in airfoil coordinates is made using Non-Uniform Rational Basis Spline (NURBS) interpolation [12], which helps ensure C^1 continuity especially near the nose, crests, and other critical regions. A stretch ratio of 1.15 is used for redistribution.

Design parameters in PARFOIL include eight parameters – camber (m), camber crest position (p), thickness (t), thickness crest position (x), leading edge radius (k), trailing edge camber (n), trailing edge camber crest position (q), and boat-tail angle (b). A parameterization is performed for two regions - a leading edge region covering from the leading edge to the camber crest, and a trailing edge region from the camber crest or pre-defined point to the trailing edge. Airfoil coordinates are typically represented by means of a polynomial [13-14]. Since PARFOIL simulates an airfoil geometry for two separated regions, C^1 continuity is imposed especially on the boundaries of the two regions.

A change in camber (m) or thickness (t) simply scales airfoil vertical coordinates in both regions. In a parametric model, camber and thickness are modified by a scaling factor (f_m) that is multiplied to the baseline value. For example, the updated camber is given by the following form:

$$m = f_m \cdot m_{BL} \tag{1}$$

In this expression, a baseline airfoil is expressed with f_m=1 (no change in camber) and a symmetric airfoil can be generated with f_m=0 (zero camber). On the other hand, when a symmetric airfoil is used as a baseline, a small value of 0.0001c is added to the camber value prior to scaling.

When any of the two crest positions (p or x) changes, the delta value of the airfoil horizontal coordinate (Δy) is added to the baseline value for the leading edge and trailing edge regions. The following is an example when a camber crest position changes from p_0 to p_1 along the horizontal axis:

$$y_p = y + \Delta y_p$$

where

$$\Delta y_p = C_3(y - p_0)^3 + C_2(y - p_0)^2 + (p_1 - p_0) \tag{2}$$

$$C_2 = -\frac{(p_1 - p_0)(1 - 3p_0 + 3p_0^2)}{(1 - p_0)^2 p_0^2}$$

$$C_3 = \frac{(p_1 - p_0)(1 - 2p_0)}{(1 - p_0)^2 p_0^2}$$

In the above expressions, y is the horizontal coordinate of the airfoil.

Similarly, when trailing edge camber increases in magnitude (Δn) or its crest position shifts from q_0 to q_1, the corresponding thickness (t_n) is updated for the trailing edge region as follows:

$$t_n(y) = t(y) + \Delta t_n$$
$$q_1 = q_0 + \Delta q$$
a) For $y_R \le y \le q_1$
$$\Delta t_n = D_3(y - q_1)^3 + D_2(y - q_1)^2 + \Delta n$$
$$D_2 = -\frac{3\Delta n}{(q_1 - y_R)^2}$$
(3) $$D_3 = -\frac{2\Delta n}{(q_1 - y_R)^3}$$
b) For $q_1 \le y \le 1$
$$\Delta t_n = E_2(y - q_1)^2 + \Delta n$$
$$E_2 = -\frac{\Delta n}{(1 - q_1)^2}$$

In the above expression, y_R is the reference position that represents a boundary point of the trailing edge region. In this study, y_R is set to 0.60c.

The thickness (t_b) due to a change in boat-tail angle is modified for the trailing edge region as follows:

$$t_b(y) = t(y) + \Delta t_b$$
(4) $$\text{where } \Delta t_b = \Delta b \cdot \frac{(y - y_R)^4}{(y_B - y_R)^4} \frac{(y-1)}{(y_B - 1)}$$

In this expression, y_B is the horizontal position where boat-tail angle is measured, and y_B is set to 0.80c in this study.

The leading edge radius (k) is defined using a correction factor (f_S) and the leading edge radius (R_{LE}) for NACA 4-digit airfoils [13-14]:

(5) $$k = f_s \cdot R_{LE} = f_s \cdot \left(1.1019 t_0^2\right) = \frac{1}{2} a_0^2$$

The upper surface thickness in the leading edge region is updated due to a change in leading edge radius using

$$t_k^u(y) = a_0\sqrt{y} + a_1 y + a_2 y^2$$
(6) $$\text{where } a_1 = \frac{2t_0}{x_0} - \frac{3}{2}\frac{a_0}{\sqrt{x_0}}$$
$$a_2 = -\frac{t_0}{x_0^2} + \frac{a_0}{2x_0^{3/2}}$$

In the above expression, t_0 is the thickness at the thickness crest position (x_0), and a_0 is calculated using Eqn. (5) in terms of t_0. The lower surface thickness can be computed similarly but with the opposite sign.

Figure 2a shows examples of morphed RC(3)-08 airfoil geometries with design parameters. It is shown that PARFOIL can generates an extensive range of parametric airfoil geometries to be used for optimization. It is worth noting that a trailing edge crest position can be used to morph a trailing edge tab or reflector design although it is not exercised in this study. Figure 2b shows an example in which the SC1095 airfoil is morphed to the RC(3)-08 airfoil. Although further tuning of the parameters could produce a closer match with the RC(3)-08, the morphed geometry is already very close to the RC(3)- 08.

C81 AIRFOIL GENERATION

With each new airfoil geometry, a C81 airfoil table needs to be generated for use as an input into a rotorcraft comprehensive analysis tool. A schematic diagram of the entire C81 airfoil table generation process is provided in Fig. 3. For the first step, PARFOIL generates morphed airfoil coordinates. A C81 patch table is then generated using C81Gen [15-16], which is a GUI wrapper comprising a 2D airfoil mesh generator and the ARC2D Navier-Stokes solver [17] (developed at the NASA Ames Research Center specifically for airfoil computations). ARC2D uses implicit finite-difference techniques to solve the two-dimensional thin-layer Navier-Stokes equations with the Spalart-Allmaras turbulence model.

The accuracy of C81Gen predictions are now examined. Figure 4 compares aerodynamic coefficients of the RC(3)-08 airfoil between the experimental data [18] and the C81Gen predictions. Experimental data is available for Mach numbers from M=0.37 to 0.90 with Reynolds numbers varied from 5.2 x 10^6 at the lowest Mach number to 9.6 x 10^6 at the highest Mach number. The predicted c_l and c_m results agree reasonably well with the experimental data up to M=0.72 and differences become noticeable at M=0.84. The predicted c_d results show relatively large offsets from the experimental data. For the predictions, a fully turbulent option was used. Figure 5 compares RC(3)-08 airfoil properties between the experimental data and the C81Gen predictions. Although only small differences are found in lift between the experimental data and the C81Gen predictions, the differences in drag are significant. For example, c_{d0} is 0.0065 at M=0.48 for the experimental data and it is 0.0077 for the C81Gen predictions.

To avoid discrepancies with measured data, a correction is made by adding the delta value to the C81Gen-generated patch table at every combination of Mach number and angle of attack in the following form:

$$C^{corr} = C^{patch} + \Delta C_{BL}$$

(7) $$\text{where } \Delta C_{BL} = C_{BL}^{\exp} - C_{BL}^{pred}$$

The subscript 'BL' indicates the baseline airfoil for which the experimental data are available. To reduce ARC2D computation time, C81Gen computations are made only for angles of attack of interest, which are typically in the range of -10 to 20 degrees. About 350 ARC2D function evaluations are made for this patched region per each airfoil table. Note that a correction for drag is taken into account by matching the experimental c_{d0} at each Mach number instead of using Eqn. (7) in order to avoid kinks in the boundaries of the patched region. The correction to C81 airfoil tables is applied to subsequent airfoil parametric studies, which are based on the RC airfoil experimental data. However, it was seen that the use of this airfoil correction does not change the overall rotor optimal design results and conclusions.

DISCUSSIONS

A full-scale wind tunnel test of a UH-60A main rotor was performed in the USAF National Full-Scale Aerodynamics Complex (NFAC) 40- by 80-foot wind tunnel at NASA Ames Research Center [19]. Figure 6 shows CAMRAD II [20] predictions of UH-60A main rotor power (STD) against the measured data (Run 52, $c_T/\sigma = 0.09$) at the NFAC facility for advance ratios of 0.15 to 0.40. For simulation, a 3-DOF propulsive trim is used with trim targets of thrust, propulsive force, and rotor roll moment. Table 1 shows trim target values in forward flight that were measured from UH-60A NFAC wind tunnel test (Run 52). The predicted rotor performance having the UH-60A standard airfoils (SC1095 and SC1094R8) appears reasonably well correlated with the measured data over a full speed range.

CAMRAD II is used for rotor performance calculations. The blade structural model is based on a beam finite element formulation with each element having fifteen degrees of freedom. In this study, each blade is modeled with five nonlinear beam elements and one rigid element inboard of the hinge. The section aerodynamics are based on lifting line theory with C81 table lookup and the ONERA EDLIN unsteady aerodynamic model. Yaw flow effects are also included. For the aerodynamic model, 23 aerodynamic panels are used with a free wake option. The time step size used is 15° in azimuth.

At high cruise speeds, rotor blades encounter transonic Mach numbers on the advancing side and experience stall or near stall at moderate Mach numbers on the retreating side. These are the key aspects of a rotor flow field that a blade designer should take into consideration. On the other hand, rotor performance improvement was found primarily from lowering profile power [11] and thus the focus here will be on profile power instead of total power.

The UH-60A rotor consists of SC1095 and SC1094R8 airfoils, denoted as the standard rotor (STD). For performance improvement, these airfoils are replaced with advanced RC airfoils (RC(3)-08 and RC(4)-10NL), which is referred to as the advanced rotor (ADV). Figure 7 displays sketches of the blades of the UH-60A standard and advanced rotors. For the advanced rotor bade, RC(4)-10NL is placed from r/R=0.735 to 0.84 and RC(3)-08 is placed from r/R=0.84 to the tip.

Figure 8 compares the contours of profile power of the UH-60A rotor having RC airfoils against SC airfoils at an advance ratio of 0.30 (Run 52, Point 31; p5231). The use of advanced RC airfoils requires less power on the advancing side where Mach numbers range 0.7 or higher (see Fig. 8b) although there is a small increase in power on the retreating side (Fig. 8d). The numerical labels in Figs. 8a, c-d indicate angles of attack and the two white circles are the boundaries of the tip and outboard airfoils.

Airfoil properties are compared in Fig. 9 between the RC airfoils and the SC airfoils. Although it displays a lower $c_{l,max}$, the RC(3)-08 airfoil shows improved airfoil characteristics in terms of M_{dd}, c_{m0}, and c_{d0} compared to the SC1095. The RC(4)-10NL airfoil also shows improved characteristics compared to the SC1094R8 airfoil. Note that drag-divergence Mach number [21] is computed using a finite difference backward scheme as

(8) $$\frac{\partial c_d}{\partial M} = 0.1$$

Figure 10 compares predicted UH-60A main rotor power over a full speed range between the standard rotor (STD), the rotor with tip RC(3)-08 (labeled as rc308-tip), and the rotor with both tip RC(3)-08 and outboard RC-410NL airfoils (ADV). Power for the rotors having RC airfoils reduces consistently over a full speed range. With the use of advanced RC airfoils, the advanced rotor (ADV) achieved a power reduction of 3.5% in hover, 10.5% at μ=0.3, and 11.0% at μ=0.4 compared to the standard rotor (STD).

Parametric Airfoil Design

Although the advanced rotor blade shows significant power reductions with the use of RC

airfoils, it is challenging to judge whether the selected RC airfoils are indeed the best choice in the design space of interest. So, further investigations are made with a series of morphed coordinates of the RC(3)-08 placed in the blade tip while keeping the RC(4)-10NL outboard without morphing.

The sensitivity of rotor power with respect to airfoil design parameters is examined. Morphed airfoil geometries are obtained by changing the values of the design parameters in a parametric airfoil model. Figure 11 shows examples of morphed airfoils with a change in camber and its crest position, along with the corresponding change in the main rotor power at μ=0.3 (p5231). For camber change, the camber scaling factor (f_m) is varied from 0 to 1.5. Similarly, the camber crest position varies from p=0.25c to 0.45c. A change in the rotor power is compared for the morphed airfoil geometries in the same figure. The change is measured from the advanced rotor (ADV) power. Although rotor power is sensitive to camber change, the advanced rotor appears to be the best configuration. On the other hand, a shift of camber crest position towards the leading edge (p=0.25c) from the baseline value (p=0.34c) reduces power by 0.7%.

Airfoil properties ($c_{l,max}$, c_{m0}, M_{dd}, and c_d) of morphed RC(3)-08 airfoils with a change in camber crest position (p) are shown in Fig. 12 and the corresponding profile power contours are given in Fig. 13. Shifting p to 0.25c (p_1) from the baseline (p=0.34c) improves $c_{l,max}$ (Fig. 12a), and generates a positive pitching moment (Fig. 12b) without sacrificing drag-divergence Mach number at lower c_L (Fig. 12c). In addition, shifting p to 0.25c produces a slightly lower c_d and so slightly lower profile power (Fig. 13) on the advancing side where high Mach numbers and negative angles of attack occur (Fig. 12e, c_d at M=0.78 and α= -2^o). On the retreating side, shifting p to 0.25c reduces profile power (Figs. 13a-c), which results from a lower c_d at moderate Mach numbers and high angles of attack (Fig. 12f, c_d at M=0.38 and α= 10^o). This power efficiency in the p1 model against the advanced RC(3)-08 model could partially result from a delay in trailing edge separation, which is observed from ARC2D-generated vorticity contours (Figs. 13d-e, at M=0.38 and α= 10^o). Interestingly, a shift of camber crest position to 0.25c shows performance benefits on both the advancing and retreating sides.

Figure 14 shows morphed airfoil coordinates with a change in thickness (t) and its crest position (x), followed by the corresponding main rotor power change at μ=0.3. Rotor power is not sensitive to a change in thickness except for a significant increase in power at the 6% thickness. The advanced RC airfoil appears close to the best choice within a tolerance range. The comparison of rotor power shows a slightly higher sensitivity with the thickness crest position. It is shown that rotor power reduces 0.7% as thickness crest position moves towards the leading edge (x= 0.30c) from the baseline advanced airfoil (x= 0.38c).

Airfoil properties of morphed RC(3)-08 airfoils with a change in thickness (t) are shown in Fig. 15 and the corresponding profile power contours at μ=0.3 are given in Fig. 16. A change in thickness significantly influences $c_{l,max}$ as expected (Fig. 15a) but impacts little on c_{m0} (Fig. 15b). The thickness change influences drag moderately. A lower thickness airfoil produces a lower c_{d0} at high Mach numbers on the advancing side (Figs. 15d-e). But, it produces a significantly higher c_d at M=0.38 and α= 10^o (Fig. 15f), which requires higher profile power on the retreating side as shown in Fig. 16.

A further sensitivity study is performed for airfoil leading edge radius. The design parameter for leading edge radius is defined in the following form:

(9) $$k = f_k \cdot k_{BL}$$

The factor f_k is a scaling factor for the leading edge radius of the morphed airfoil, and k_{BL} is the leading edge radius of the baseline airfoil. Figure 17 shows morphed airfoil coordinates with a change in leading edge radius and also shows the corresponding main rotor power change at μ=0.3. As leading edge radius changes, rotor power shows a small sensitivity except at f_k=0.5. The value of f_k = 1.2 yields slightly less profile power.

Airfoil coordinates in the trailing edge region can be altered by augmenting trailing edge camber or boat-tail angle. To augment the trailing edge camber, a constant value (Δn) is added to the baseline trailing edge camber. Similarly, boat-tail angle is augmented by adding a constant value (Δb) to the baseline boat-tail angle. Figure 18 shows morphed airfoil coordinates with changes in trailing edge camber as well as boat-tail angle, followed by the corresponding main rotor power change at μ=0.3. Although rotor power is not sensitive to a change in trailing edge camber, the minimum power value seems near the advanced airfoil. Rotor power appears slightly more sensitive to boat-tail angle. Reducing boat-tail angle by 2 to 4 degrees would reduce rotor power by 0.4 and 0.3% from the advanced airfoil, respectively. It is noted that the parameter of trailing edge crest position is not exercised in the parametric study.

New Configurations for Performance Design

The power required for the advanced rotor is found frequently to be at a near minimum in the sensitivity study. Investigations are further

extended in order to find better configurations that require lower power than the advanced rotor configuration. For this investigation, two members of the ptx9kb family will be chosen based on the outcomes in the previous sensitivity study.

The ptx9kb family consists of a series of ptx9kb airfoils that vary thickness crest position (x9) while the active design parameters (p, t, k, and b) stay at good design values and the inactive parameters (m and n) are at the baseline default values. Thus, thickness crest position (x) varies from 0.25c to 0.45c while the active parameters are set to p=0.25c, t=7%, f_k=1.2, and b= -4^o and the inactive parameters are set to f_m=1.0, Δn=0, and Δq=0. Figure 19 shows morphed airfoil coordinates of the ptx9kb family, followed by the corresponding main rotor power change measured from the advanced rotor power. Interestingly, rotor power in the ptx9kb family are always lower by 1% or more compared to the advanced rotor.

Among the ptx9kb family, two configurations (Conf1=ptx2kb, Conf2=ptx4kb) are chosen for detailed comparison. The Conf1 model is a member of the ptx9kb family with x=0.30c and the Conf2 model is with x=0.40c. Their morphed airfoil coordinates are shown in Fig. 20, along with the advanced RC(3)-08 airfoil (ADV) and the p_1 model (ADV with p=0.25c). The main rotor power comparison shows that the p_1 model seems a primary contributor to power reduction. The two Conf1 and Conf2 models show further reductions over a full range of flight speeds except for hover. For Conf1 and Conf2, the power reduction is 1.0 and 1.4% at μ=0.3, and 2.7 and 2.9% at μ=0.4 from the advanced rotor configuration (ADV), respectively, although there is a slight increase of 0.2 and 0.3% in hover. These results are compared again in Fig. 21 but against the predicted standard rotor (STD) power. The comparison shows power reductions in a full range of speeds including hover and is very encouraging. The Conf1 and Conf2 models reduce rotor power by 3.2 and 3.3% in hover, 11.3 and 11.7% at μ=0.3, and 13.6 and 13.4% at μ=0.4 relative to the STD rotor, respectively.

Airfoil properties between Conf1 and Conf2 are compared in Fig. 22. With a placement of thickness crest towards the leading edge, Conf1 shows slightly higher $c_{l,max}$ and lower M_{dd} compared to Conf2 (Figs. 22a and 22c). It is interesting to observe that the Conf1 c_{d0} is lower than the Conf2 at M=0.78 and then it reverses the trend resulting in a higher c_{d0} at M=0.84 (Fig. 22d), which is also seen in Fig. 22e at negative angles of attack. On the retreating side Conf1 produces a lower drag at moderate Mach numbers and high angles of attack compared to Conf2 (Fig. 22f).

Figure 23 compares the contours of rotor profile power at μ=0.3 between Conf1 and Conf2 and the difference of Conf2 profile power against Conf1. On the advancing side, Conf2 is favorable for power reduction due to its thickness crest position placed towards the mid-chord. On the retreating side, Conf1 is favorable due to its thickness crest position placed towards the leading edge.

Maneuvering Flight Constraint

The UTTAS high-g pull-up maneuver condition (C11029) in the UH-60A Airloads Flight Test program [22] is used to investigate the maximum design load on the pitch link. The UTTAS maneuver begins near the maximum level flight speed, and achieves a normal load factor (2.1g) that significantly exceeds the steady-state lift limit of the rotor. After about 40 revolutions (9.4 seconds), the aircraft returns to steady-state flight (0.65g). The pitch link loads (oscillatory time history, mean, and half peak-to-peak) are compared with flight data in Fig. 24. The comprehensive analysis prediction displays a time delay by 3-4 rotor revolutions. The mean prediction shows a constant offset to the flight data, and the half peak-to-peak pitch link load displays under-prediction by 38%. This prediction shortcoming is due to the lower fidelity models in comprehensive analysis and can be overcome by employing CFD/CSD coupled analyses [23-24]. Although the shortcoming in the prediction is not trivial, the comprehensive results can still be useful because they show a reasonably accurate trend of the pitch link load response in maneuvering flight, with which the maximum design loads could be estimated for the UTTAS maneuver.

Pitch link load responses of Conf1 and Conf2 are examined for the same UTTAS high-g pull-up condition. Figure 25 shows oscillatory time history of pitch link load of the Conf1 and Conf2 rotors. The mean and half peak-to-peak pitch link loads are compared in Fig. 26 against the standard rotor (STD). Even though the Conf1 and Conf2 rotors reduce rotor power significantly, their half peak-to-peak pitch link loads increase by about 8.5% from the standard rotor. This increase is not favorable and should be considered as a constraint during rotor blade design.

CONCLUDING REMARKS

In a framework of rotor optimization, a parametric airfoil design tool, PARFOIL, has been developed with design parameters of camber and camber crest position, thickness and its crest position, leading edge radius, trailing edge camber and its crest position, and boat-tail angle.

Rotor performance is improved significantly by 3.5% in hover, 10.5% at μ=0.3, and 11.0% at μ=0.4

for the UH-60A advanced rotor (ADV) having RC(3)-08 and RC(4)-10NL airfoils instead of the original SC1095 and SC1094R8 airfoils.

A sensitivity study for rotor performance is successfully performed by varying the design parameters of the RC(3)-08 airfoil from the UH-60A advanced rotor design (ADV). Only small improvements in performance are achieved from the advanced rotor design by morphing the RC(3)-08 geometry. The most influential design parameter is camber crest position, and it shows a power reduction of 0.7% as it shifts towards the leading edge (p= 0.25c) from the baseline value (p= 0.34c).

Two configurations, Conf1 and Conf2, are used to seek further performance improvement from the UH-60A advanced rotor design. Based on the outcomes in the sensitivity study, these configurations are determined using a combination of various design parameters – camber crest position, thickness and its crest position, leading edge radius, and boat-tail angle. Rotor performance improvements made with Conf1 and Conf2 are 3.2 and 3.3% in hover, 11.3 and 11.7% at μ=0.3, and 13.6 and 13.4% at μ=0.4, respectively, compared to the original standard rotor. This demonstrates the ability of PARFOIL to find better airfoils in the design space.

Pitch link load responses of the two configurations are examined for the UTTAS high-g pull-up condition. Even though the Conf1 and Conf2 rotors reduce power significantly, their half peak-to-peak pitch link loads increase by about 8.5% from the original standard rotor value. This increase is not favorable and should consider as a design constraint during rotor blade design.

ACKNOWLEDGMENTS

The author would like to express many special thanks to Wayne Johnson, NASA Ames Research Center, for his invaluable insights, guidance, and encouragement on development of a parametric airfoil design tool. The author would also like to express special thanks to William Polzin, Sukra Helitek, Inc. for providing invaluable supports on using the C81Gen software.

REFERENCES

[1] Colucci, F., “Technology for the Next Flight,” *Vertiflite*, January/February 2017, pp. 14-17.

[2] Hirschberg, M., “JMR Advances Towards Flight Under Cover of Darkness,” *Vertiflite*, Marvh/April 2017, pp. 12-13.

[3] Moffatt, S. and Griffiths, N., “Structural Optimisation and Aeroelastic Tailoring of the BERP IV Demonstrator Blade,” Proceedings of the American Helicopter Society 65th Annual Forum, Grapevine, Texas, May 27-29, 2009.

[4] Schneider, S., Heger, R., and Konstanzer, P., “Cheeseman Award Paper: BLUECOPTER™ Demonstrator: the State-of-the-Art in Low Noise Design,” Proceedings of the AHS 73rd Annual Forum, Fort Worth, Texas, May 9-11, 2017.

[5] Sobieczky, H., “Parametric airfoils and wings,” *Recent Development of Aerodynamic Design Methodologies*, Springer, 1999, pp. 71-87.

[6] Kulfan, B. M., “Universal Parametric Geometry Representation Method,” *Journal of Aircraft*, Vol. 45, No. 1, January-February 2008, pp. 142-158.

[7] Poole, D. J., Allen, C. B., and Rendall, T. C. S., “Metric-Based Mathematical Derivation of Efficient Airfoil Design Variables,” *AIAA Journal*, Vol. 53, No. 5, May 2015.

[8] Masters, D. A., Taylor, N. J, Rendall, T. C. S., Allen, C. B., and Poole, D. J., “Review of Aerofoil Parameterisation Methods for Aerodynamic Shape Optimisation,” Proceedings of the 53rd AIAA Aerospace Sciences Meeting, Kissimmee, Florida, January 2015.

[9] Samareh, J. A., “Multidisciplinary Aerodynamic - Structural Shape Optimization Using Deformation (MASSOUD),” Proceedings of the 8th AIAA/USAF/NASA/ISSMO Symposium on Multidisciplinary Analysis and Optimization,” Long Beach, California, September 2000.

[10] Wang, L., Diskin, B., Biedron, R. T., Nielsen, E. J., Sonnerville, V., and Bauchau, O. A., “High-Fidelity Multidisciplinary Design Optimization Methodology with Application to Rotor Blades,” Proceedings of the AHS International Technical Meeting on Aeromechanics Design for Transformative Vertical Flight, San Francisco, California, January 2018.

[11] Lim, J. W., “Consideration of Structural Constraints in Passive Rotor Blade Design for Improved Performance,” *The Aeronautical Journal*, 120 (1232), October 2016; also appeared as an invited Cheeseman Award paper in the Proceedings of the AHS 71st Annual Forum, Virginia Beach, Virginia, May 2015.

[12] Piegl, L, and Tiller, W., “The NURBS Book,” Springer-Verlag, 2nd edition, 1997.

[13] Abbott, I. H. and Doenhoff, A. E., *Theory of Wing Sections*, Dover Publications, Inc., 1959.

[14] Ladson, C. L., Brooks, Jr., C. W., Hill, A. S., and Sproles, D. W., “Computer Program to Obtain Ordinates for NACA Airfoils,” NASA TM 4741, December 1996.

[15] Rajagopalan, R. G, Baskaran, V., Hollingsworth, A., Lestari, A., Garrick, D., Solis, E., and Hagerty, B., “RotCFD - A Tool for Aerodynamic Interference of Rotors: Validation and Capabilities,” Proceedings of the American Helicopter Society Future Vertical Lift Aircraft Design Conference, January 18-20, 2012, San Francisco, California.

[16] Koning, W. J. F., Johnson, W., and Allan, B. G., "Generation of Mars Helicopter Rotor Model for Comprehensive Analyses," Proceedings of the AHS International Technical Meeting on Aeromechanics Design for Transformative Vertical Flight, San Francisco, California, January 2018.

[17] Pulliam, T. H., "Efficient Solution Methods for the Navier-Stokes Equations," *Lecture Notes for the Von Karman Institute for Fluid Dynamics Lecture Series*, Brussels, Belgium, Jan. 1986.

[18] Noonan, K. W., "Aerodynamic Characteristics of a Rotorcraft Airfoil Designed for the Tip Region of a Main Rotor Blade," NASA TM-4264, AVSCOM TR-91-B-003, May 1991.

[19] Norman, T. R., Shinoda, P., Peterson, R. L. and Datta, A., "Full-Scale Wind Tunnel Test of the UH-60A Airloads Rotor," Proceedings of American Helicopter Society 67th Annual Forum, Virginia Beach, Virginia, May 3-5, 2011.

[20] Johnson, W., "Rotorcraft Aerodynamic Models for a Comprehensive Analysis," Proceedings of the 54th Annual Forum of the American Helicopter Society, Washington, D.C., May 20-22, 1998.

[21] Johnson, W., *Rotorcraft Aeromechanics*, Cambridge University Press, 2013.

[22] Bousman, W. G., and Kufeld, R. M., "UH-60A Airloads Catalog," NASA TM-2005-212827, August 2005.

[23] Bhagwat, M.J., and Ormiston, R.A., "Examination of Rotor Aerodynamics in Steady and Maneuvering Flight Using CFD and Conventional Methods," American Helicopter Society Specialist's Conference on Aeromechanics Proceedings, San Francisco, CA, January 2008.

[24] Roget, B., Sitaraman, J., Wissink, A., Saberi, H., and Chen, W., "Maneuvering Rotorcraft Simulations Using HPCMP CREATE™-AV Helios," Proceedings of the 54th AIAA Aerospace Sciences Meeting, San Diego, California, January 2016.

Table 1. Trim targets in forward fight that were measured from UH-60A NFAC test (σ =0.0826)

μ	Shaft angle deg	C_T/σ	-X/q ft^2	M_{ROLL} lbs-ft
0.151	0.89	0.0902	20.0	-408
0.200	-0.31	0.0902	22.9	-716
0.240	-1.50	0.0903	24.2	-957
0.300	-3.50	0.0905	24.7	-1670
0.350	-5.58	0.0906	25.6	-2591
0.370	-6.74	0.0907	25.8	-2834
0.386	-7.57	0.0908	26.1	-3021
0.400	-7.60	0.0907	23.2	-3203

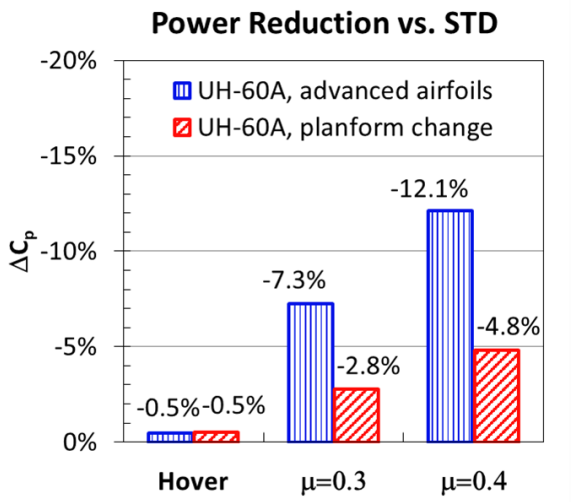

Figure 1. Effects of advanced airfoils and planform change on UH-60A rotor performance. The delta values are measured against the UH-60A standard rotor.

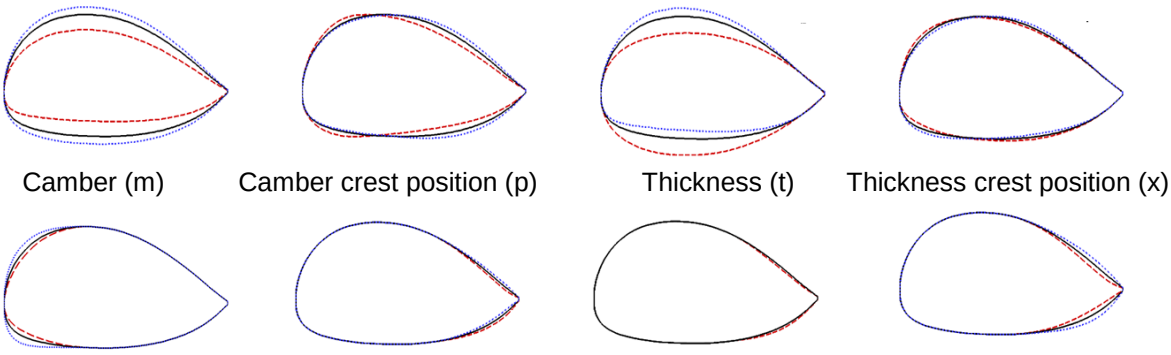

a) Morphed airfoil coordinates with design parameters

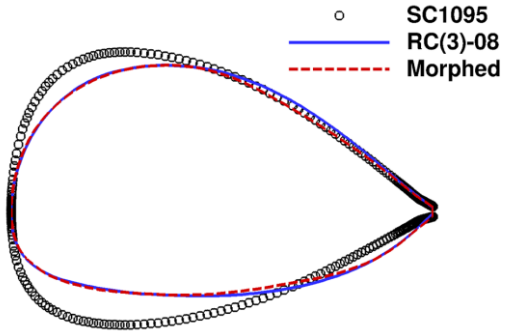

b) Morphed airfoil coordinates after SC1095 airfoil morphs to RC(3)-08

Figure 2. RC(3)-08 airfoil coordinates with design parameters (vertical scale enlarged).

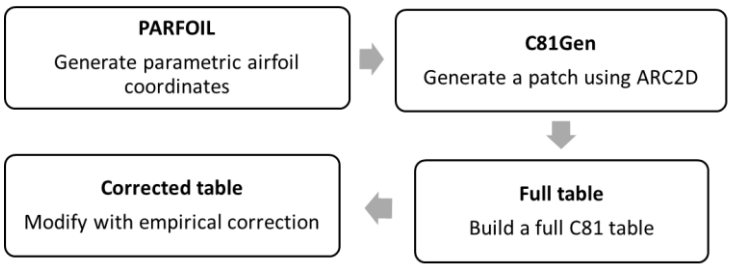

Figure 3. Parametric airfoil table generation process.

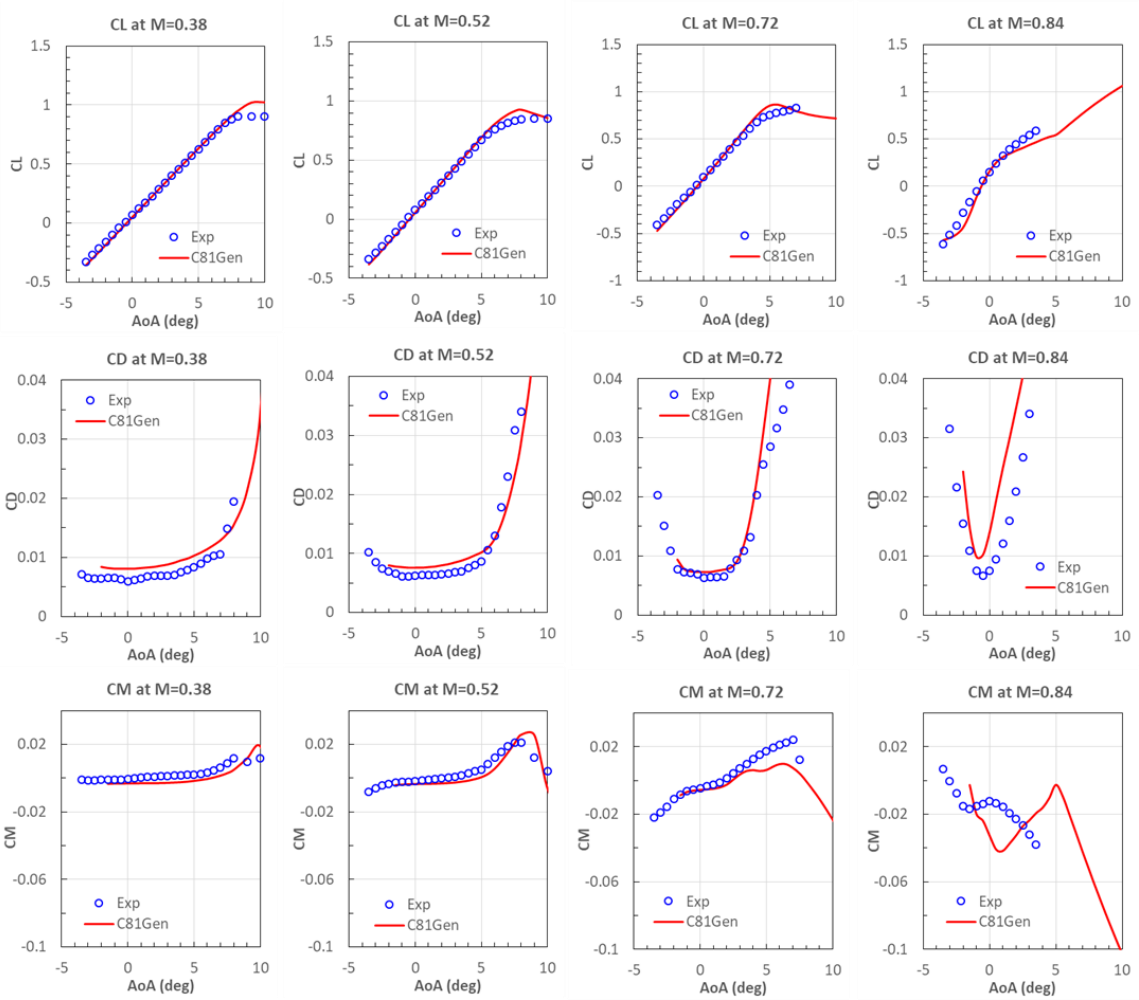

Figure 4. Comparison of RC(3)-08 aerodynamic coefficients between the experimental data and C81Gen-predicted results without corrections.

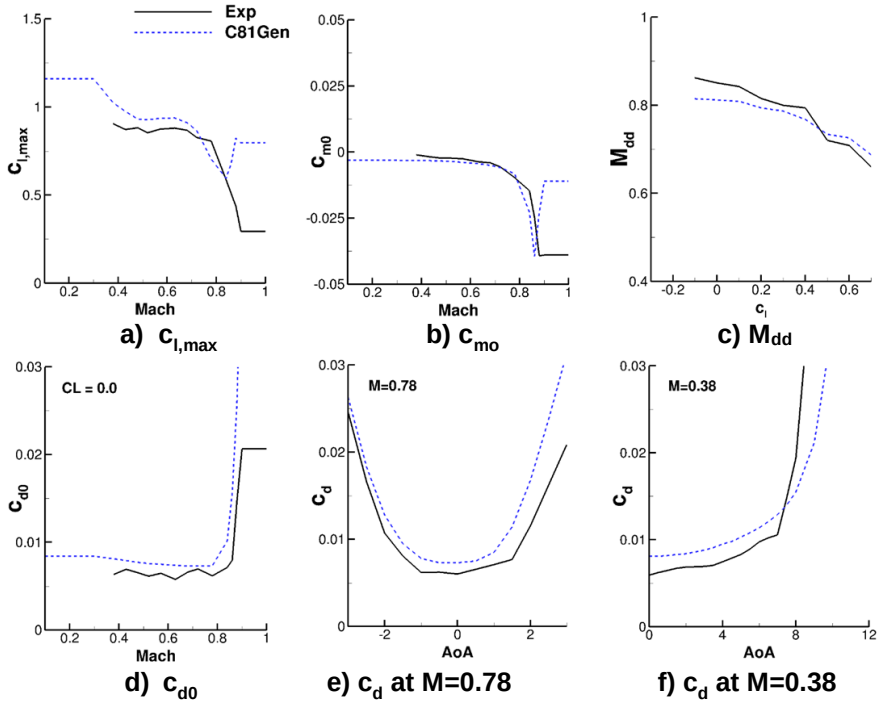

a) $c_{l,max}$ b) c_{mo} c) M_{dd}

d) c_{d0} e) c_d at M=0.78 f) c_d at M=0.38

Figure 5. Comparison of RC(3)-08 airfoil properties between the experimental data and C81Gen-predicted results without corrections.

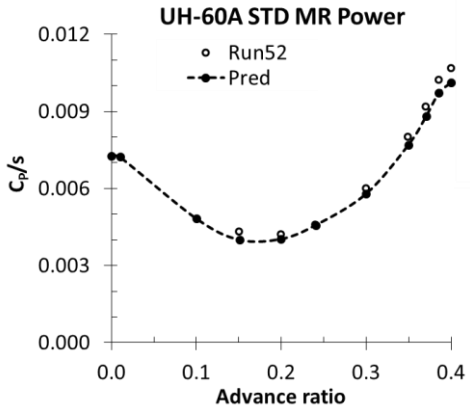

Figure 6. Correlation of the UH-60A standard main rotor power polar in a full speed range.

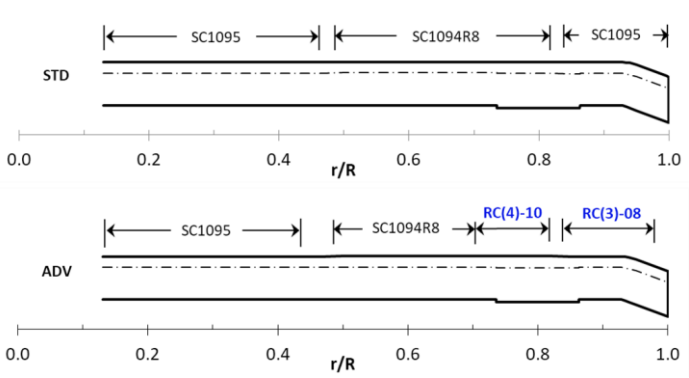

Figure 7. Sketches of the UH-60A standard blade (STD) and advanced blade having RC airfoils outboard (ADV).

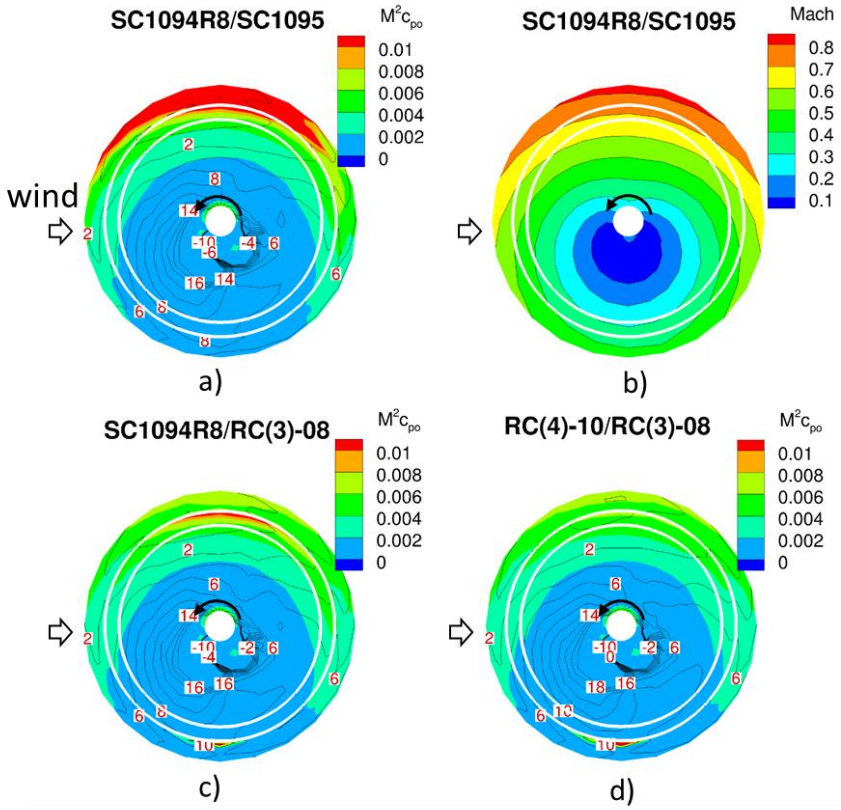

Figure 8. Comparison of profile power of the UH-60A rotor having a variation of airfoils at μ=0.30 (p5231). The numerical labels indicate angles of attack and the two white circles are the boundaries of RC tip and outboard airfoils. a) Power, Standard, b) Mach numbers, Standard, c) Power, Tip with RC(3)-08, and d) Power, Tip with RC(3)-08 and outboard with RC(4)-10NL.

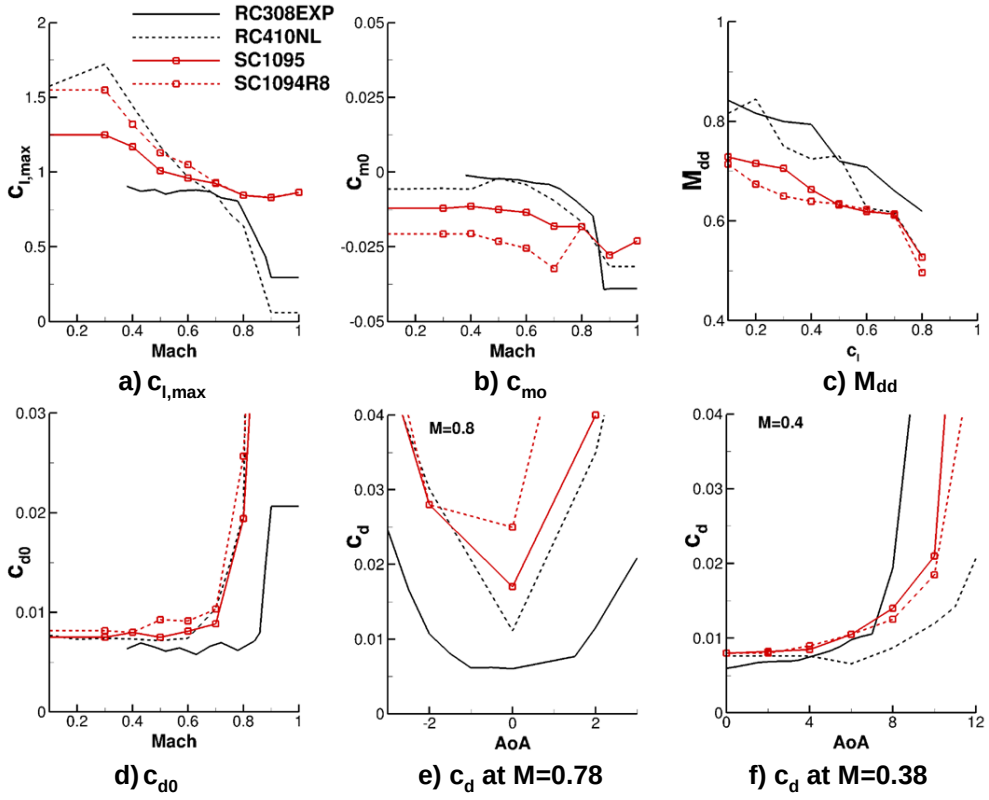

Figure 9. Comparison of airfoil properties between RC(3)-08, RC(4)-10, SC1095, and SC1094R8.

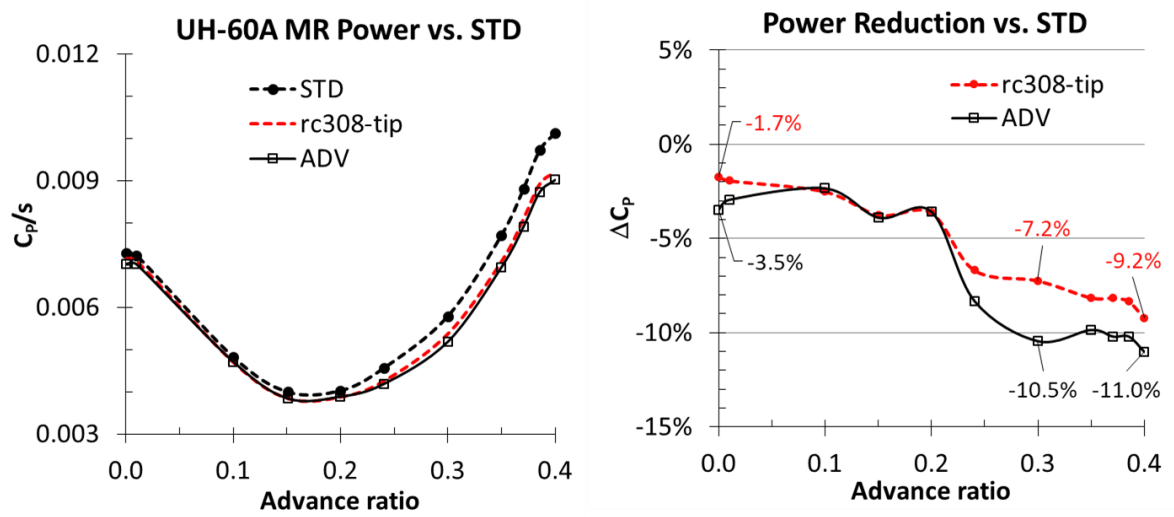

Figure 10. Comparison of predicted power of the UH-60A rotor having the standard blade (STD), the blade with the tip RC(3)-08 airfoil (rc308-tip), and the blade with the tip and outboard RC airfoils (ADV).

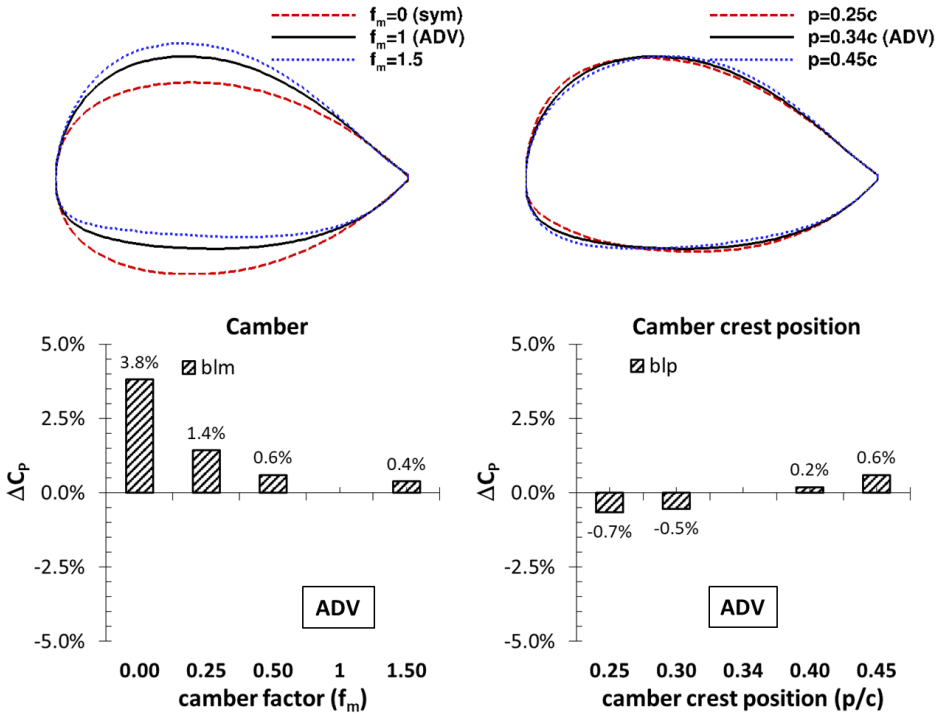

Figure 11. Morphed RC(3)-08 airfoil coordinates with changes in camber (m) and camber crest position (p) and their power reductions at μ=0.30 (p5231). Vertical scale of airfoil coordinate enlarged.

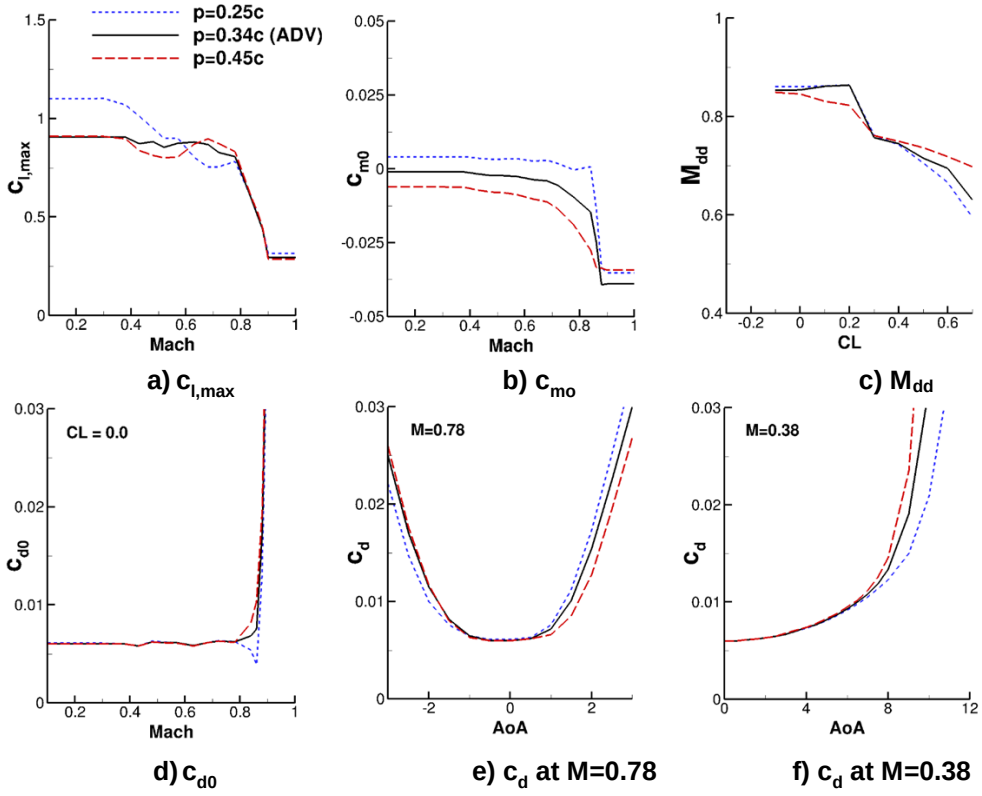

Figure 12. Airfoil properties of morphed RC(3)-08 airfoils with a change in camber crest position (p).

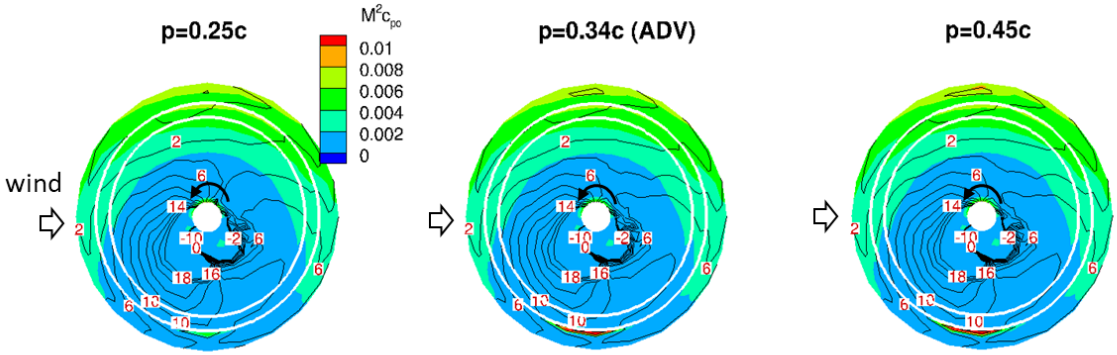

Profile power: a) p=0.25c b) p=0.34c c) p=0.45c

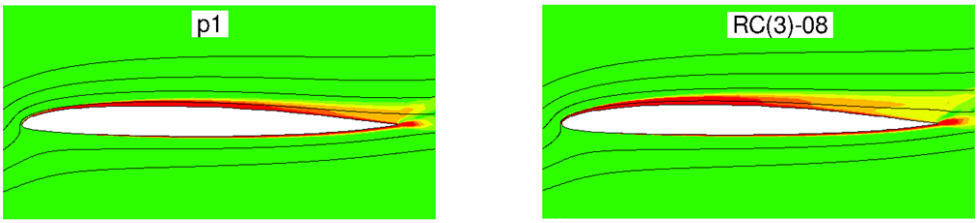

Max. vorticity at M=0.38 and α=10°:
d) p=0.25c (p1) e) p=0.34c (ADV)

Figure 13. Profile power of morphed RC(3)-08 airfoils with a change in camber crest position (p) at μ=0.30 (p5231) and its vorticity contours around the tip airfoils.

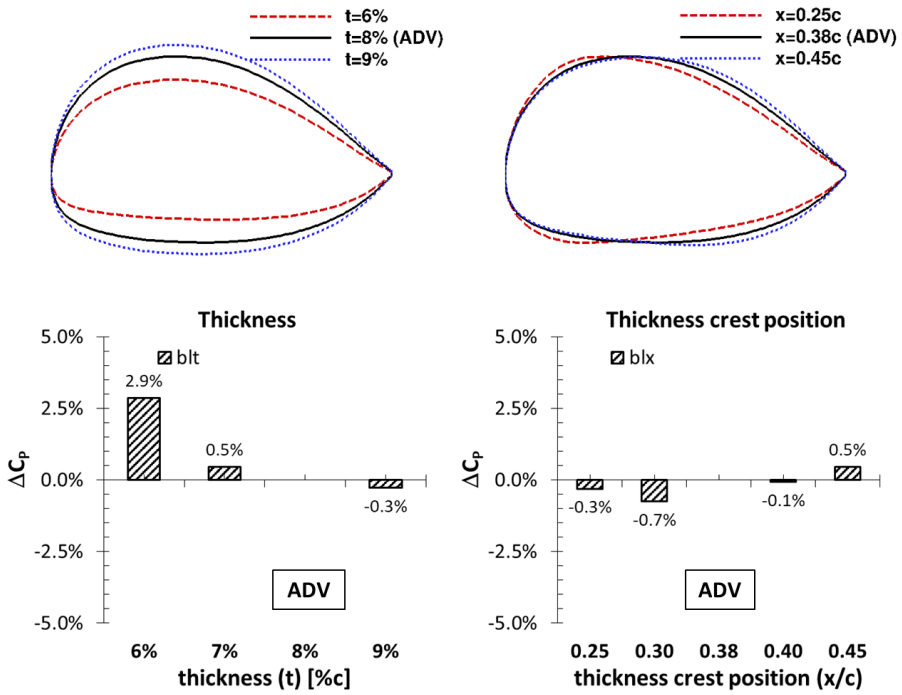

Figure 14. RC(3)-08 airfoil coordinates with changes in thickness (t) and thickness crest position (x) and their power reductions at μ=0.30 (p5231). Vertical scale of airfoil coordinates enlarged.

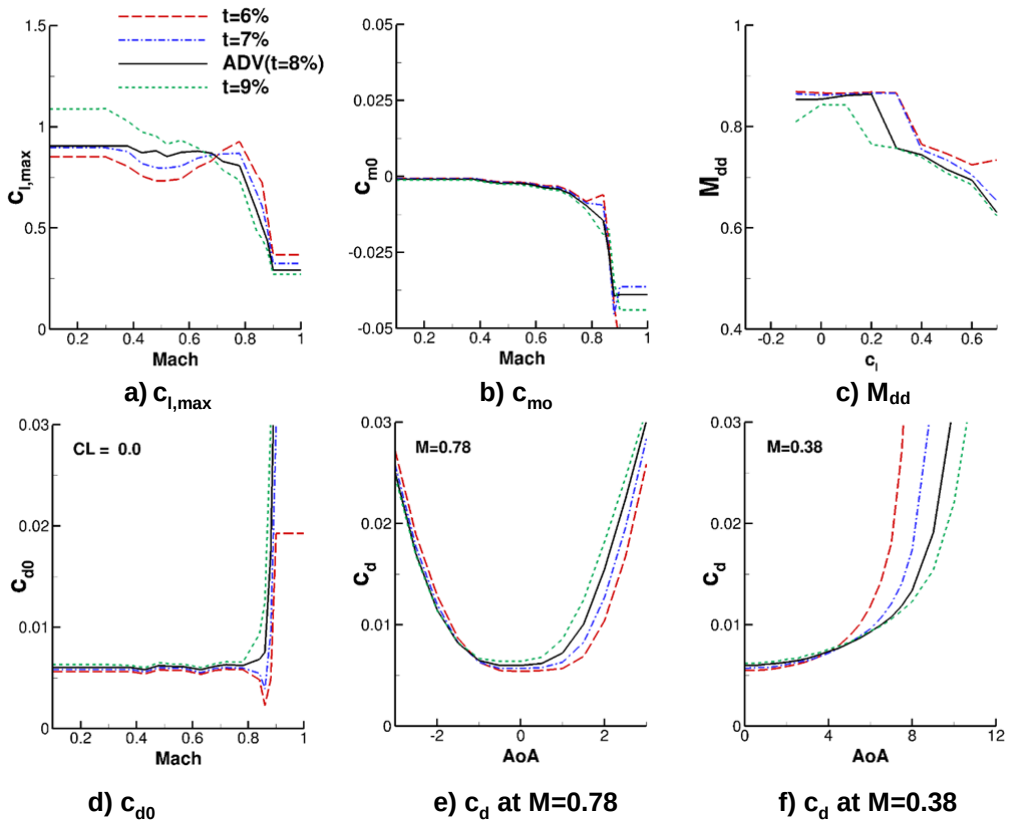

Figure 15. Properties of morphed RC(3)-08 airfoils with a change in thickness (t).

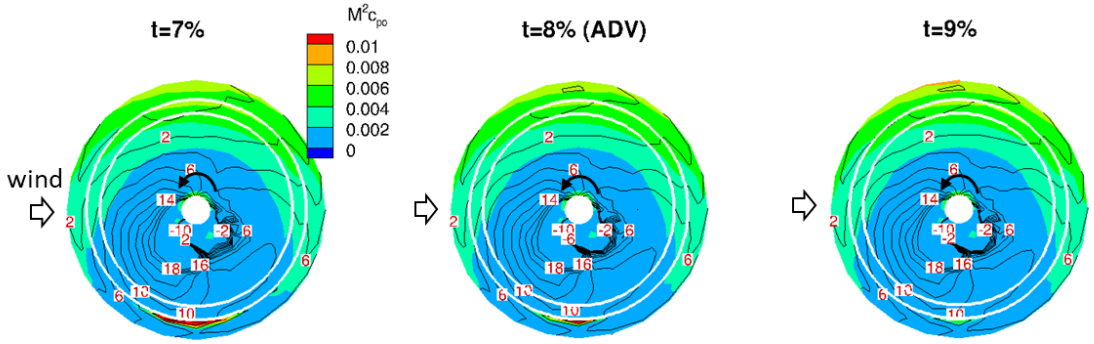

Figure 16. Profile power of morphed RC(3)-08 airfoils with a change in thickness (t) at μ=0.30 (p5231).

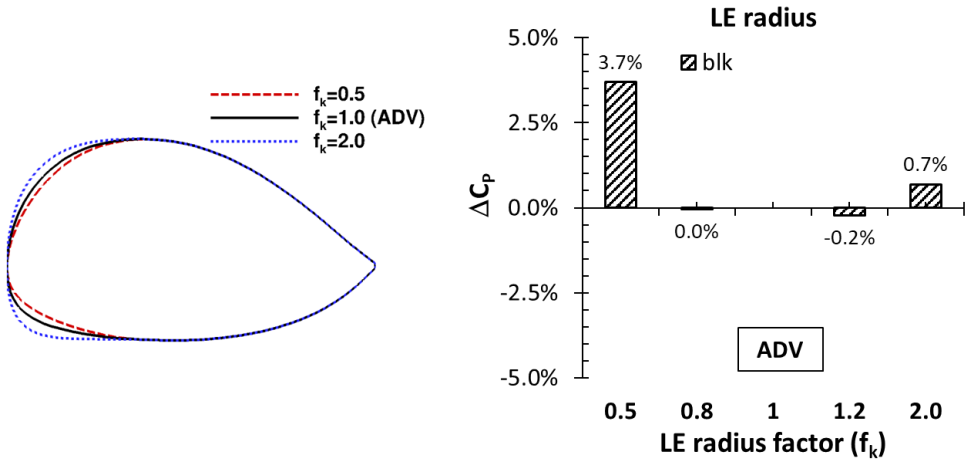

Figure 17. Morphed RC(3)-08 airfoil coordinates with a change in leading edge radius (k) and their power reductions at μ=0.30 (p5231). Vertical scale of airfoil coordinates enlarged.

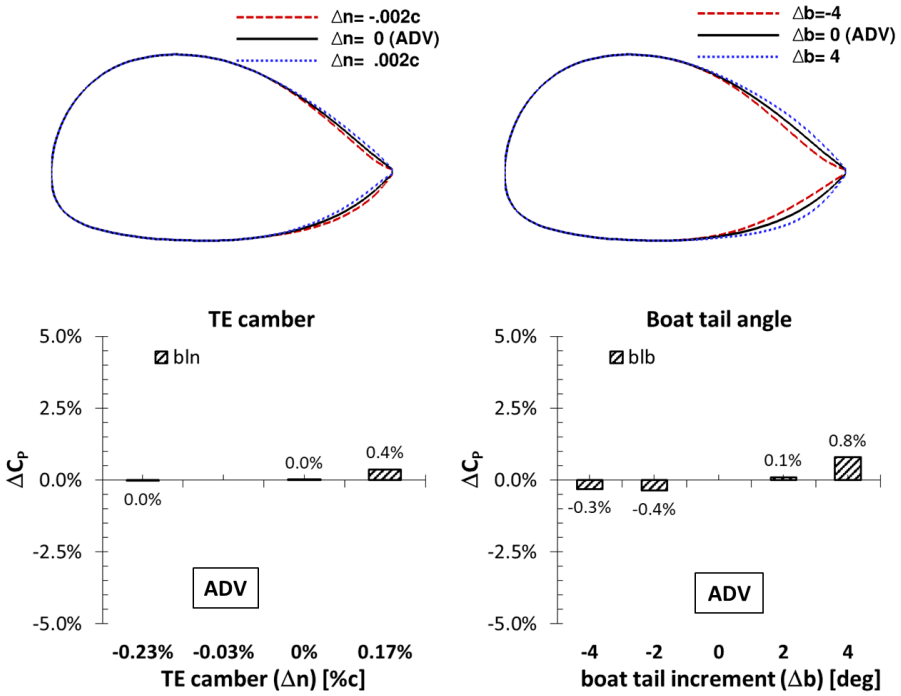

Figure 18. RC(3)-08 airfoil coordinates with changes in trailing edge camber (n) and boat-tail angle (b), and their power reductions at μ=0.30 (p5231). Vertical scale of airfoil coordinates enlarged.

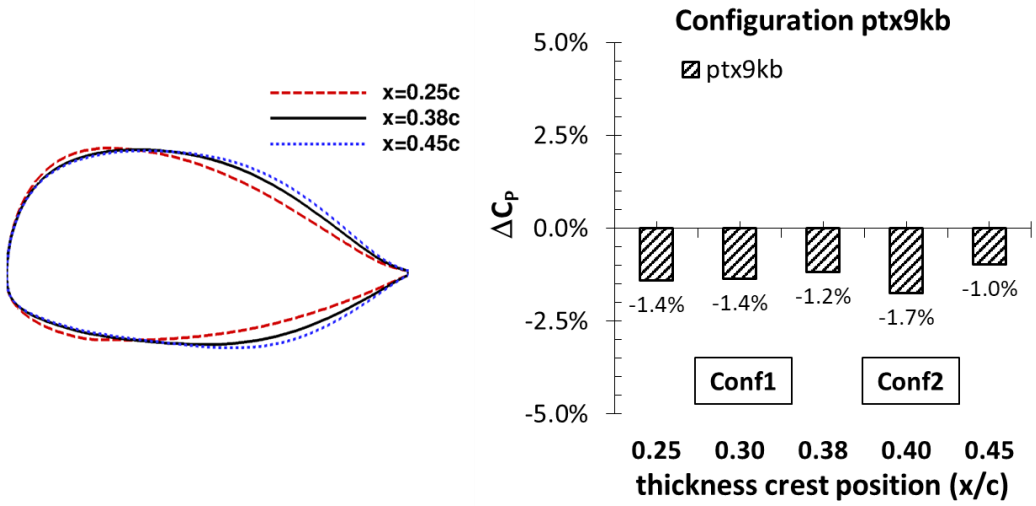

Figure 19. The ptx9kb family airfoil coordinates with a change in thickness crest position (x) and their main rotor power change from the advanced rotor at μ=0.30 (p5231). Vertical scale of airfoil coordinates enlarged.

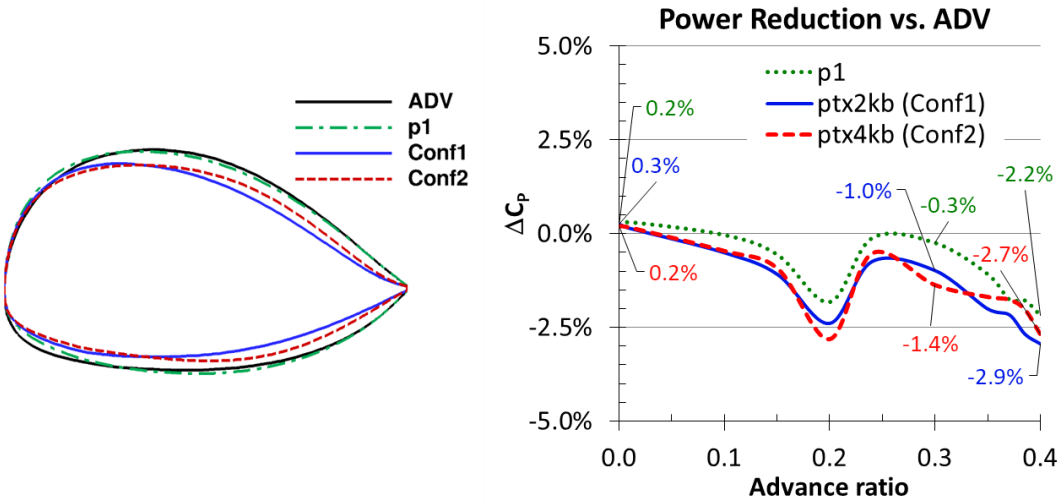

Figure 20. Conf1 (ptx2kb) and Conf2 (ptx4kb) airfoil coordinates along with the advanced and p1 (advanced with p=0.25c) models and their power reductions against the advanced rotor (Run 52). Vertical scale of airfoil coordinates

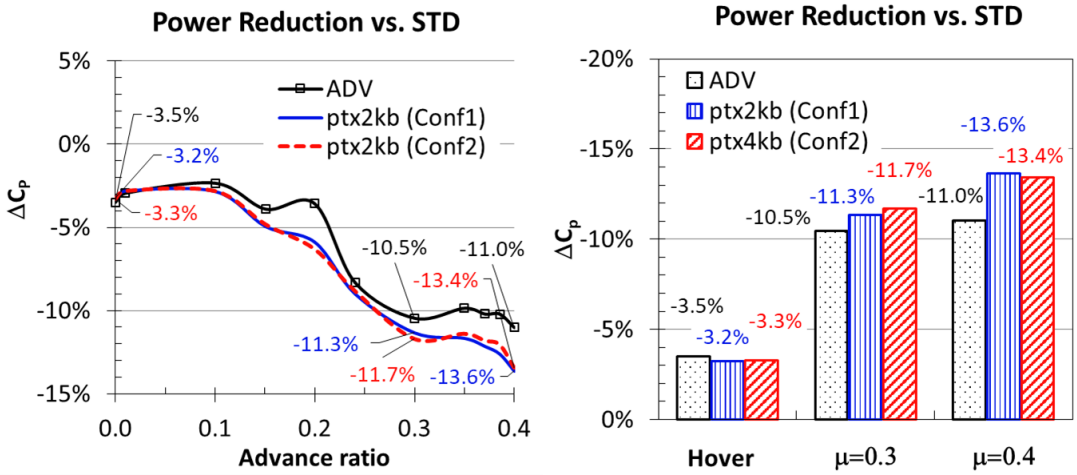

Figure 21. Power reductions of the Conf1 and Conf2 rotors against the standard rotor in a full speed range.

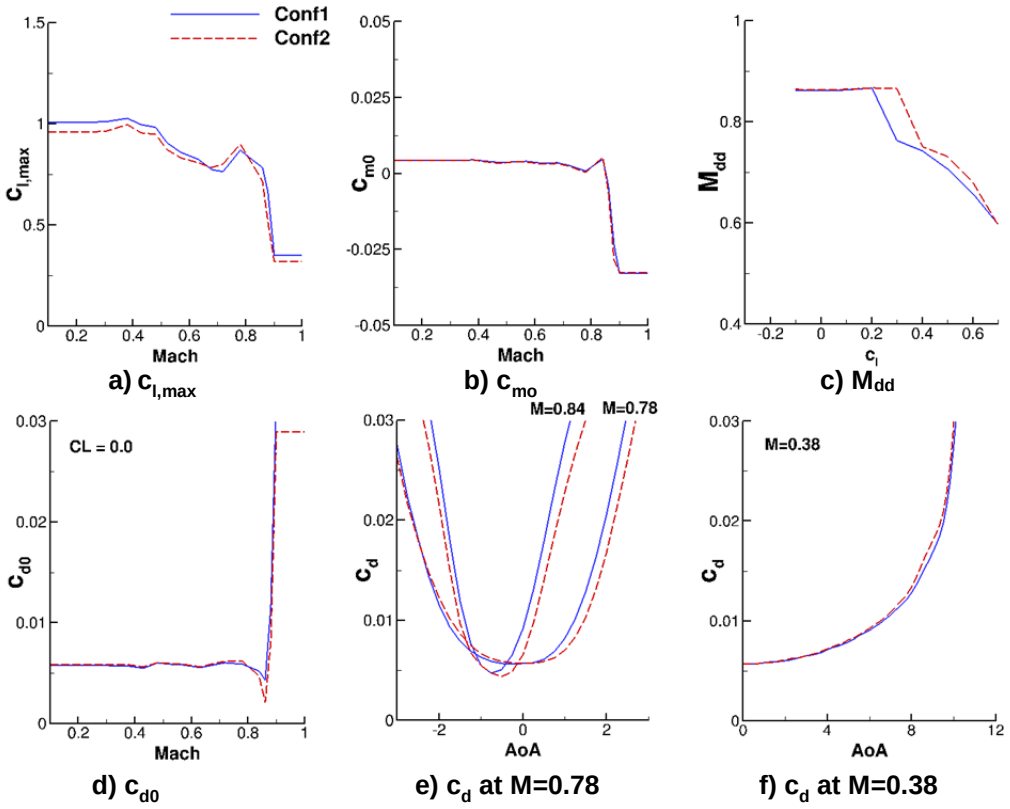

Figure 22. Properties of the Conf1 and Conf2 airfoils at μ=0.30 (p5231).

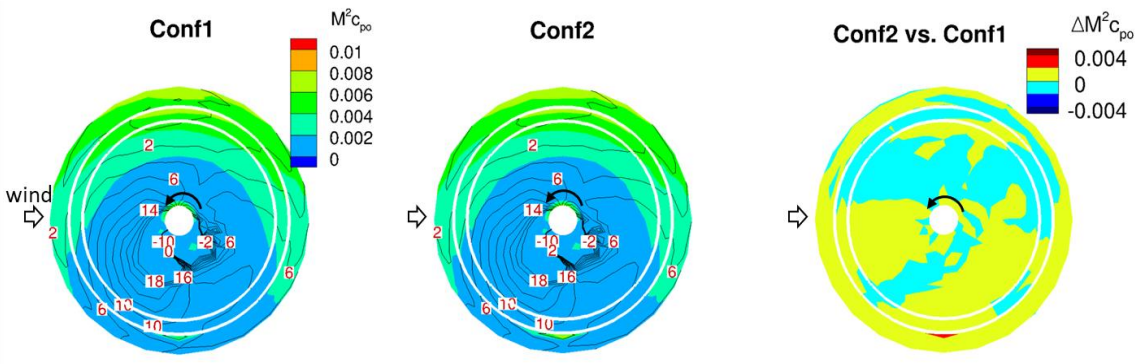

Figure 23. Profile power of the Conf1 and Conf2 rotor configurations at μ=0.30 (p5231).

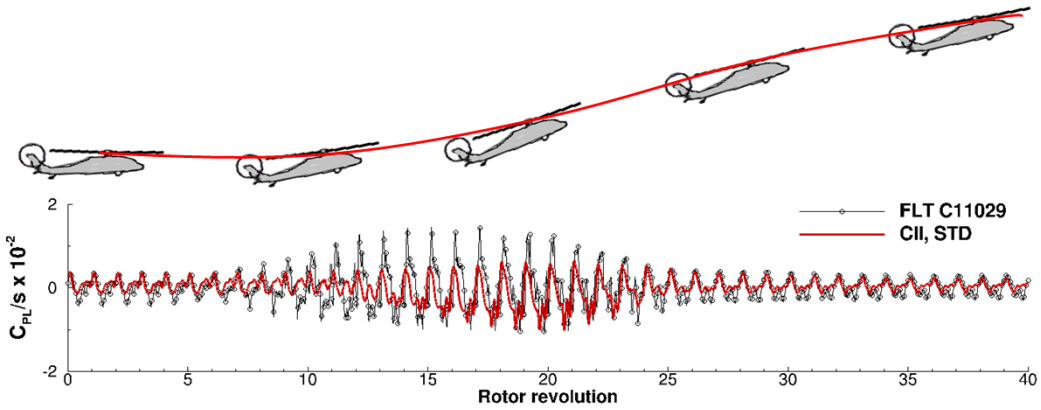

a) Oscillatory time history

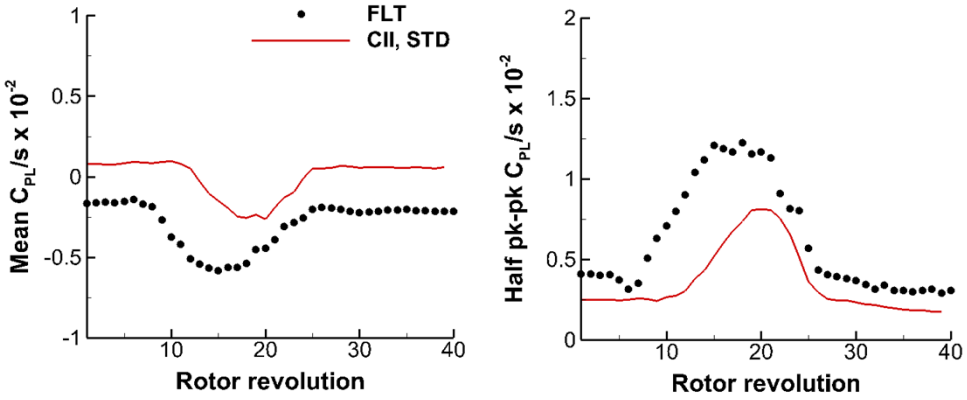

b) Mean

c) Half peak-to-peak

Figure 24. Correlations of a) Oscillatory time history, b) mean, and c) half peak-to-peak of pitch link load of the UH-60A rotor during the UTTAS maneuver (C11029).

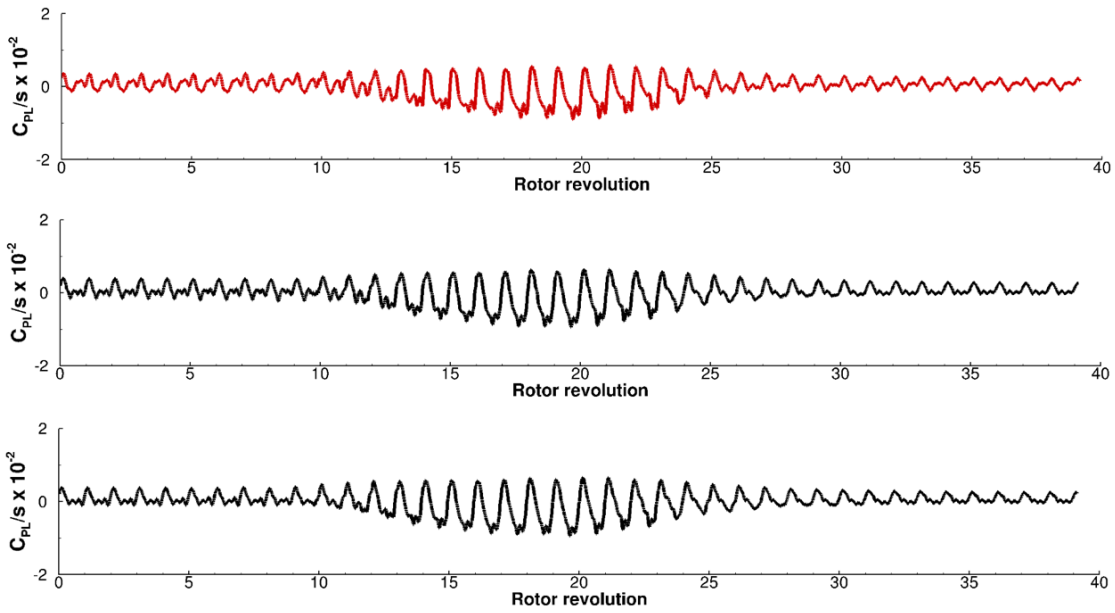

Figure 25. Oscillatory time history of pitch link load of the UH-60A rotor during the UTTAS maneuver (C11029) for the standard, Conf1, and Conf2 rotors.

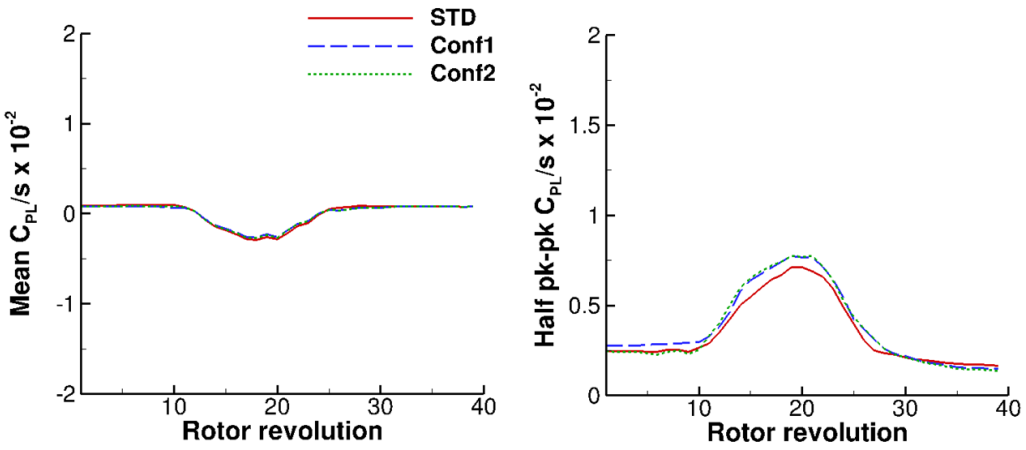

a) Mean **b) Half peak-to-peak**

Figure 26. Mean and half peak-to-peak of pitch link load of the UH-60A rotor during the UTTAS maneuver (C11029) for the standard, Conf1 and Conf2 rotors.